Microstructure characterisation of nanocomposite polymeric foams by X-ray microtomography

Erwan Plougonven[1], Pierre Marchot[1], Christophe Detrembleur[2], Tran Minh Phuong[2], Angélique Léonard[1]

[1]Department of Applied Chemistry, University of Liège, Belgium, eplougonven@ulg.ac.be
[2]Center for Education and Research on Macromolecules, University of Liège, Belgium

ABSTRACT

Recent advances in microstructured materials have given rise to many new types of composites that exhibit original and interesting physical properties. For example, a nanocomposite made of carbon nanotubes inside a polymer matrix shows exceptional electromagnetic interference shielding effectiveness when foamed. However, the effective properties of such materials strongly depend on the shape and topology of the microstructural cells. An accurate method for investigating the cellular microstructure is X-ray microtomography (XRμT), for it is non-destructive, and it provides 3D geometric information. Although it cannot be used to observe nanofiller dispersion, it has a strong potential for cell structure characterization.

In order to reduce the need for trial and error for tailoring these materials, our objective is to characterize, using XRμT, two different types of foaming procedures, namely supercritical CO_2 batch foaming and freeze drying. As the resolution is limited compared to cell size, we have developed a novel statistical method based on 3D autocorrelation to determine characteristic length and examine anisotropy. We present results for these two types of foams and show the limitations of this method.

Keywords Polymeric foam; Nanocomposites; Microtomography; Autocorrelation

1 INTRODUCTION

Electric circuits, which function at ever higher frequencies, are responsible for much of the increased electromagnetic pollution. These electromagnetic interferences (EMI) are detrimental to electronic appliances as well as living tissue, as it can cause radiative damage. This begs the need for more efficient EMI shielding solutions. Many applications are concerned, from commercial or industrial electronic systems, to military, telecommunications and antenna systems (Ho-Chul et al. 2006). One common solution is the use of metal sheets, but it has the inconveniences of being heavy, prone to corrosion, difficult to manufacture and difficult to tune its shielding effectiveness (SE), and reflecting most of the electromagnetic energy back on the circuits instead of absorbing it. Therefore an optimised shielding has high SE and low reflectivity. For the former the material needs to have a high electric conductivity (hence the use of metal), and for the latter a low dielectric constant, or rather one that is closer to the surrounding air.

In order to reduce this difference in dielectric constants, an alternative to metal sheets is foamed materials, as the high amount of porosity reduces this difference. Polymers are a good candidate for foaming, as they are cheap, lightweight, and easy to mould. Among them, poly(ϵ-caprolactone) (PCL) or polymethyl methacrylate (PMMA), present the highest conductivities, although largely insufficient to avoid most of the electromagnetic energy from traversing it. For increasing conductivity, a conductive nanofiller is added, carbon nanotubes (CNT). CNTs have several advantages: they have a high aspect ratio (<1000) meaning that conductive networks are formed in the matrix with a lower filler percentage, which is important as this addition increases the dielectric constant. They also benefit the mechanical properties and thermal conductivity of the material (Molenberg et al. 2010).

The microstructure of the foamed composites has an influence on the EMI absorption, and therefore accurate characterisation of the porous structure is needed. A traditional method is mercury porosimetry, however this technique provides a simplified view of the structure, and is not well suited for some polymeric foams, which shrink under the pressure (Maquet et al. 2003). More accurate characterisation requires an imaging technique to observe the structure and image analysis to perform measurements. Scanning Electron Microscopy (SEM) is commonly used, but more recently X-Ray

microtomography (XRμT) show potential, as it is non-destructive and provides a full 3D volume view of the structure (Baruchel et al. 2000, Blacher et al. 2002, 2006, Leonard et al. 2008).

We first present the material preparation and initial measures performed on SEM scans, then show microtomographic acquisitions and describe the autocorrelation function. Finally we present the results on these foams and show the problems encountered with this method.

2 MATERIALS AND PRIOR METHODS

Two different foaming processes are studied, freeze-drying and super-critical CO_2 batch foaming. Different polymers are better suited for each process, namely PCL for the former and PMMA for the latter.

Freeze-drying is called so because of the solvent sublimation at low temperature. The polymer is first mechanically mixed with 1wt. % CNTs in a Brabender mixer for 5 minutes at 90°C and 60 rpm. The mixture is then dissolved in dioxane (to a ratio dioxane/mixture of 10/1) in a 30-minute mechanical agitation at 80°C. The CNTs are further dispersed in an ultrasound bath for 30 minutes. This solution is quickly cooled by liquid nitrogen for 15 minutes in order to freeze the structure. It is then placed in a vacuum for 48 h at -15°C so that the solvent sublimates and is removed. Finally, in order to avoid heat fracturation, the sample is slowly brought back to room temperature (+2° per hour). Figure 1 shows SEM scans of this material. The drying process generates a strongly anisotropic open-celled structure, which then translates into anisotropic SE, which shows the importance of characterising this anisotropy.

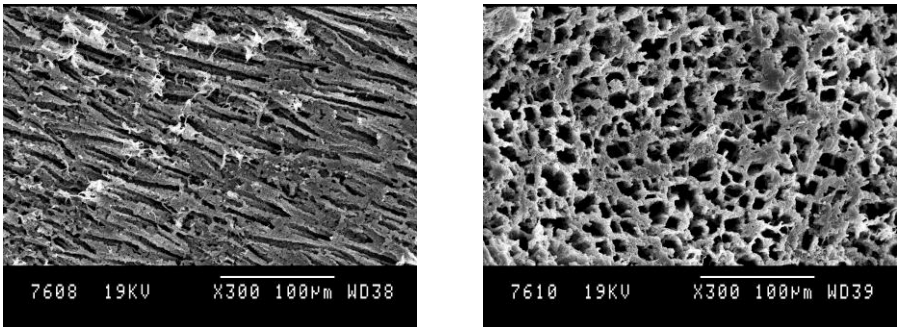

Figure 1: Perpendicular SEM images of the PCL foams produced by freeze-drying.

The second process begins in the same way, a mechanical mixing of the polymer, PMMA in this case, with the CNTs (4 wt. %) under the same conditions. The mixture is then placed in a high-pressure and temperature (150 b, 120°C) chamber where super-critical CO_2 ($scCO_2$) will impregnate it for 16h. Once the mixture is saturated with $scCO_2$ the pressure is quickly released so the impregnated $scCO_2$ expands and forms a closed-cell and highly regular porous structure. Cell wall thickness and cell size can be controlled by varying the temperature and pressure conditions during $scCO_2$ saturation. Figure 2 shows a SEM scan of such a material. From these images, an automatic cell separation method was developed, a simple image processing using classical methods (gradient, distance map, watershed). For each cell, the number of pixels that comprise it are counted, and cell cross-sectional surface area distributions are determined. However, these results, although indicative of the cell sizes, have strong limitations. Firstly, this is a 2D process (a cell is not necessarily cut at its diameter). Secondly, we notices many cell walls that are ripped and pierced, this introduces further errors (underestimation) in the cell sizes. Finally, the thickness of some walls is such that the process also separates wall portions.

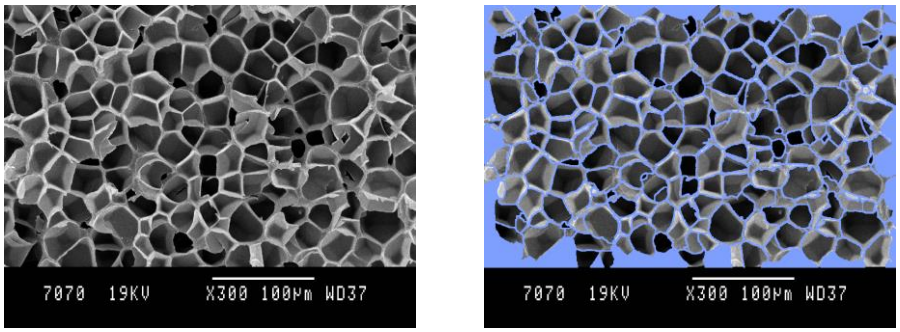

Figure 2: SEM of a PMMA composite with 4 wt.% of CNTs. The right image shows an automatic separation method used to measure cell sizes.

Although several methods exist to reduce these limitations (advances in stereology, size filtration using a priori information), XRµT was used to further investigate these materials.

3 MICROTOMOGRAPHY AND AUTOCORRELATION

Tomography is the non-invasive process of generating images of cross-sections from a series of transmission or reflection data acquired by illuminating the object from different directions. In the case of X-ray tomography, for each direction of illumination, the process is similar to a radiography: the acquired transmission data gives an attenuation map of the rays. The amount of energy absorbed will depend on the atomic number of the element traverse, its density, and the ray energy. The problem is then to reconstruct a 3D X-ray attenuation map from the radiograms. In cone-beam geometries of laboratory microtomographs, the Feldkamp reconstruction algorithm is most commonly used (Feldkamp et al. 1984).

3.1 Setup and acquisition

The foams are cut into centimetre-sized samples and scanned using a Skyscan 1172 microtomograph (Kontich, Belgium), with settings producing images with pixel size close 5 µm. The X-ray source is set at 60 kV, and radiograms are taken every 0.1° over 360°. The reconstruction is then made with Skyscan's NRecon software, generating a 3D image of roughly 1800^3 pixels. Figure 3 presents a reconstruction of the PMMA foam at the *low* resolution of 6.91 µm / pixel. We see when zooming in (right image) that the resolution, far lower than SEM, is insufficient for a direct segmentation and cell separation (local measures), therefore a global method was developed and investigated.

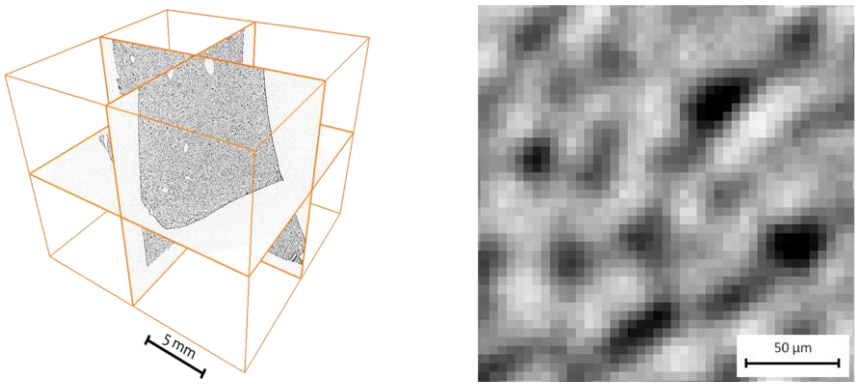

Figure 3: XRµT reconstruction of a PMMA foam containing 4 wt.% of CNTs. The left image shows the complete volume with three perpendicular cross-sections, and the right image is a zoom on a cross-section. The lighter pixels represent the porous phase.

3.2 Autocorrelation

There are two main types of global measurements found in the literature: intercept methods and autocorrelation. Intercept methods, such as Mean Intercept Length (MIL) or Intercept Segmentation Deviation, which are part of the standard grain measurement methods of set by the American Society for Testing and Materials since 2001, are based on using lines at several positions and angles and their traversal of the object. They involve counting the number of times the lines pass through the porosity, and the length of those traversals. Another type of global measurement is autocorrelation, which gives a similarity measure in the volume as a function of distance and direction. It consists in a cross-correlation of the image with itself, and is less used in 3D applications. Autocorrelation is compared with the MIL by Wehrli et al. (2006), who favors autocorrelation because of its speed and lesser sensitivity to noise. More importantly, the image needs not to be segmented in order to use autocorrelation.

Autocorrelation of a signal X_t is the cross-correlation of that signal with a translated version of itself, written $X_{t+\tau}$. The autocorrelation for a given value τ is defined as follows:

$$R(\tau) = \frac{E[(X_t - \mu)(X_{t+\tau} - \mu)]}{\sigma^2} \quad (1)$$

Where *E* is the expected value operator, μ the mean, and σ^2 the variance. Since this procedure is applied on a 3D image, the translation has three components, and the resulting correlation is itself 3D, written $R(\tau_x, \tau_y, \tau_z)$. The average autocorrelation at a given distance *d* of translation (for all translations τ such that $\sqrt{\tau_x^2 + \tau_y^2 + \tau_z^2} = d$) indicates whether there is a particular order at that distance.

If autocorrelation is calculated for all possible translations, and the average value is plotted as a function of distance, the variations are representative of the 3D structure. For regular and uniform structures such as regular packings, a clear peak can be seen at a distance corresponding to the diameter of the packed objects. For non-regular structures, such as our composite foam, we rather examine the interval of values of the autocorrelation at a given distance. Indeed, the deviation of the maximum correlation from the average value, which is non-zero because the autocorrelation is computed on a finite volume (and our material is never *purely irregular*), becomes greater around characteristic lengths in the image. This gives an indication of the average distance between cells in our composite, which corresponds to the cell diameter plus the wall thickness.

In order to plot these values as a function of translation distance, autocorrelation is examined at a finite set of points on a sphere. This set of points v_i is defined by the vertices of a triangulated sphere whose centre *c* is at the zero translation, and generated by a simple subdivision technique of an octahedron, as in figure 4. In this paper, we use triangulations of 16572 vertices. Furthermore the measurements are made at a finite set of distances, each distance value separated by the size of one pixel from the next.

Figure 4: Generation of the set of directions examined for the rose diagram. The method begin with an octahedron (left) and iteratively subdivides the edges and projects the generated vertices onto a sphere, obtaining 18 vertices at step 1 (centre), 66 vertices at step 2 (right), etc.

Figure 5 shows the resulting plots of the maximum correlation deviation as a function of distance, in a 1mm^3 subvolume taken at the centre of the foam samples. The representativeness of a 1 mm^3 volume

has been established by examining the convergence of the average autocorrelation for increasing subvolume sizes. The measured values are represented by the markers, and the peaks in these functions are determined by using a spline interpolation in between these markers. We find values of 15 and 18 µm for the PCL and PMMA foams, respectively. This estimated intercell distance is in good agreement with a visual inspection of the SEM scans. For the anisotropic PCL foam, this value obviously corresponds to the distance between cells perpendicular to their tubular structure, as it is in that direction that autocorrelation varies most.

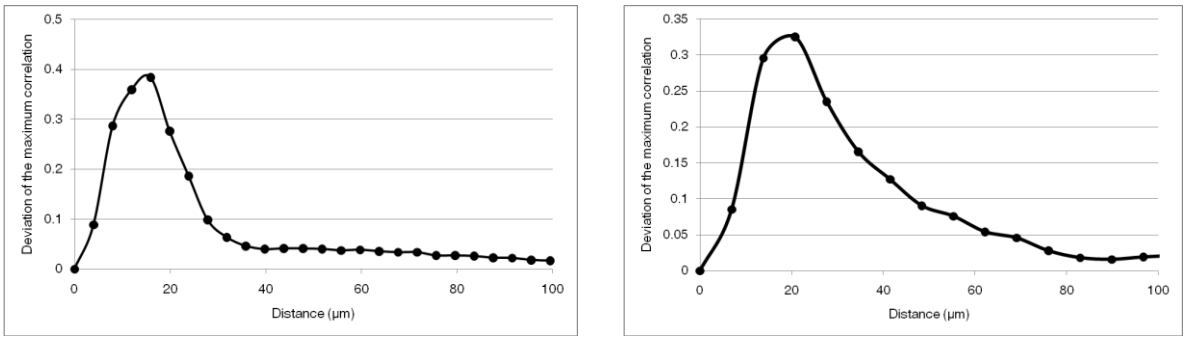

Figure 5: Deviation of the maximum correlation from the mean value as a function of distance for (left) the PCL foam shown in figure 1 and (right) the PMMA foam shown in figure 2. The markers correspond to the distances computed.

We clearly see that this is a powerful technique to measure average characteristic lengths, even at very small length scales relative to the pixel size (for the PMMA foam, the peak is detected at 2.66 pixels). Furthermore, this method can be used to detect anisotropies in the materials, although some problems do emerge, as is described in the following section.

3.3 Rose diagram and anisotropy

The triangulated spheres illustrated in figure 4 can be used to map the autocorrelation values in particular directions. If the autocorrelation values are directly examined only at the surface of this sphere, and especially for small values (relative to the pixels) in our case, the grid effects from the pixels overwhelms the variations from the material, as seen in figure 6.

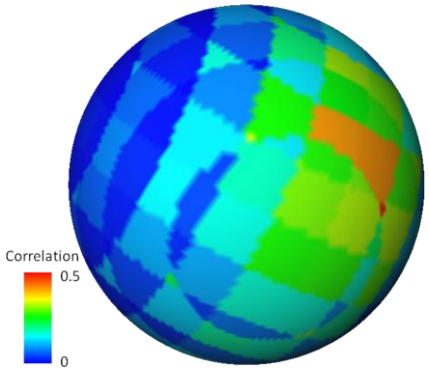

Figure 6: Autocorrelation values, for the PCL sample, on the sphere of radius 4 pixels (near the peak of the maximum correlation deviation).

In order to reduce this grid effect, we integrate the autocorrelation values over a range *[d₁,d₂]* of distances. To do so in all directions $\overrightarrow{cv_i}$, we examine the segments $\left[l_1^i, l_2^i\right]$, where l_1^i is the point at a distance d_1 of the centre, in the direction $\overrightarrow{cv_i}$, and l_2^i is at a distance d_2 in the same direction. For the integration, we sum up the products of the autocorrelation values of the pixels *p* through which $\left[l_1^i, l_2^i\right]$ passes (a pixel is considered as a unit cube) and the length of the segment portion inside each pixel,

$\left| p \cap \left[l_1^i, l_2^i \right] \right|$, and divide this sum by the total length of the segment. We therefore have, for each point v_i, the integrated value:

$$R'(v_i) = \frac{\sum_{p \cap \left[l_1^i, l_2^i \right] \neq \varnothing} R(p).\left| p \cap \left[l_1^i, l_2^i \right] \right|}{\left\| \overrightarrow{l_1^i l_2^i} \right\|} \quad (2)$$

Figure 7 illustrates a few definitions used for the previous equation. Returning to the PCL sample, if we integrate the autocorrelation over a range of 2 pixels around the peak observed in figure 5, i.e. the range [2,6], we obtain a much smoother set of values, as illustrated in figure 8. Naturally the range of *R'* is lower than for *R* as the strong discontinuities from pixel to pixel are averaged.

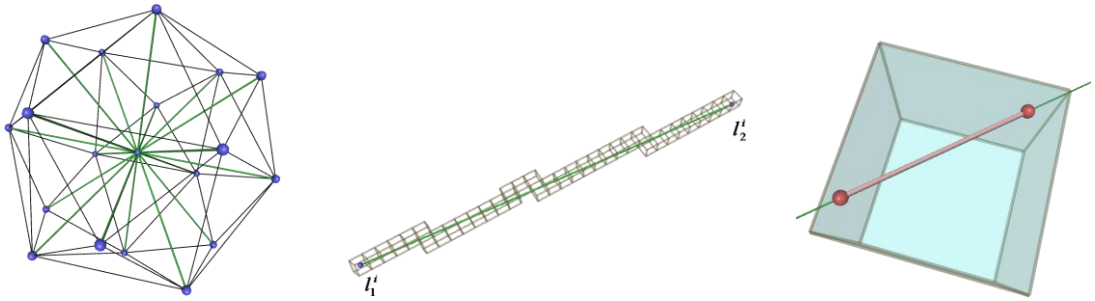

Figure 7: From left to right: wireframe view of the sphere with the vertices v_i in blue and all the examined directions in green; one segment $\left[l_1^i, l_2^i \right]$ along which the autocorrelation is integrated, along with the set of pixels that intersect it; intersection of $\left[l_1^i, l_2^i \right]$ with a pixel *p* in red, with its bounds marked by red spheres.

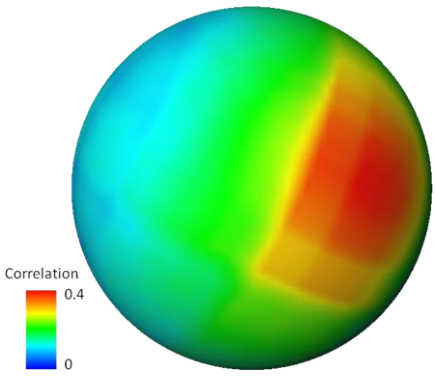

Figure 8: Autocorrelation integration, for the PCL sample, in the range [2-6], in pixels, i.e. around the peak of the maximum correlation deviation.

Finally, in order to highlight preferential directions shown by R', the vertices v_i are moved along the direction $\overrightarrow{cv_i}$ according to their respective values $R'(v_i)$, so that the new distance of v_i from c becomes

$$\left\| \overrightarrow{cv_i} \right\| + a.\left(R'(v_i) - \left\langle R' \right\rangle \right) \quad (3)$$

Where $\left\langle R' \right\rangle$ is the average value of R' for the given range, and *a* is a scaling factor to accentuate the variations. The resulting shape is called a rose diagram.

The rose diagram for the PCL sample is displayed in figure 9. The point of view is slightly different from that of figure 8 in order to better understand the 3D shape. We also overlap the 1 mm^3 XRµT subvolume from which *R'* was computed, and perpendicular oblique cross-sections, in the directions shown by the rose diagram, are extracted. We clearly observe that the principal axis of the rose diagram is in the average direction of the cell elongations. This can lead to the computation of an anisotropy field inside the whole sample if *R'* is computed over all subvolumes of the XRµT reconstruction.

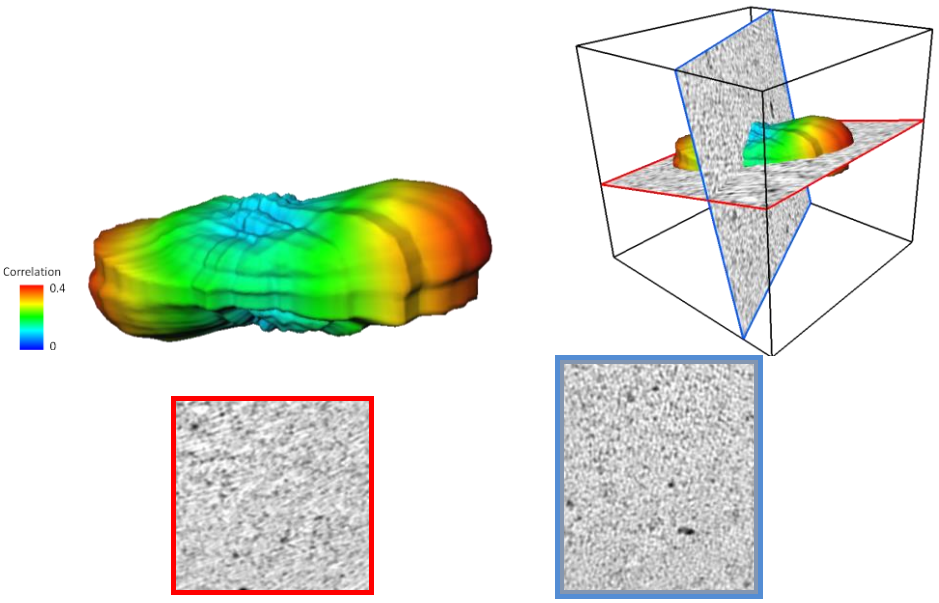

Figure 9: Rose diagram for the PCL sample, using a scaling factor *a* of 30. The top row shows the rose diagram on the left, and on the right the rose overlapped with the 1 mm^3 subvolume of the sample from which it was calculated. Two oblique perpendicular cross-sections are displayed, the red along the direction in which R' is highest, and the blue perpendicular to that direction. The bottom row shows these two cross-sections.

Unfortunately, this idea is hindered by the fact that the rose diagram, although insensitive to random noise, can prove oversensitive to directional artefacts in the XRµT reconstruction. Indeed, the same process applied to the PMMA sample, supposed isotropic because perpendicular SEM images revealed no differences, shows the similar amounts of anisotropy. Figure 10 shows its rose diagram, with a range for *R'* of [0,5] pixels, around the peak of the maximum correlation deviation of 2.77 pixels, and a scaling factor of 30. This time, the preferential directions of the rose are perfectly diagonal in the XY axis of the XRµT volume. This is a strong indication that artefacts from the tomographic scanning or reconstruction process strongly affect the rose diagram. This hypothesis is confirmed by additional scans of the same sample placed differently in the microtomograph, and the rose diagrams seen affected by this position, and not only by the intrinsic structure of the material.

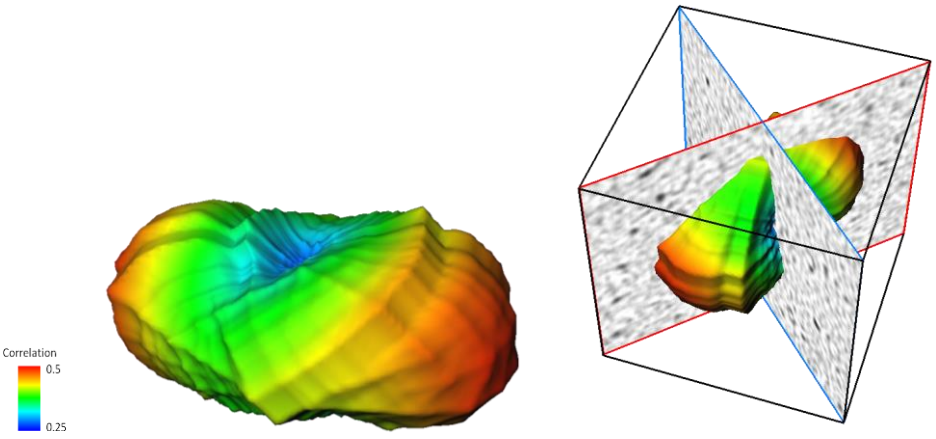

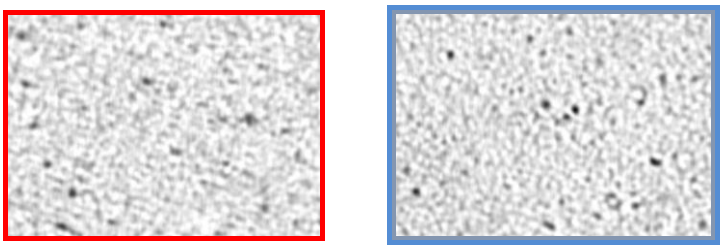

Figure 10: Rose diagram for the PMMA sample. Again, perpendicular oblique cross-sections, in the directions indicated by the rose diagram, are shown in the bottom row.

There are several reasons why such artefacts come about: movement of the setup, either from the sample or the X-ray source, or bad rotation alignment. The sample can move during the scanning because of mechanical imprecisions of the rotation stage, a bad attachment of the sample on the holder, or even the deformation of the sample from the heat inside the chamber. Indeed, the X-ray target (the tungsten plate hit by the electron beam and that generates X-rays) heats up during a scan, and if one increases the magnification, i.e. bring the sample closer to the X-ray source, these effects can become important. For the same reason (heating of the target) the X-ray source, considered as a fixed mathematical point in the Feldkamp reconstruction scheme but in reality resembling a ellipsoid a few microns wide, will shift and possibly deform during a long scan. Finally, the reconstruction considered that the rotation axis is perfectly centred and vertical in the radiograms, though in practice it is not. This can be well corrected using prior scanning of a calibration phantom and post-examination of the radiograms.

Unfortunately for the study of the foams, there is no way of knowing to which extent these artefacts influence the measure of anisotropy in the structures.

4 CONCLUSIONS AND PERSPECTIVES

Foamed polymer composites reinforced by CNTs are a promising solution for effective EMI shielding material. Not only is nanotube dispersion important in regards to shielding effectiveness, but so is pore shape and size distributions. In order to fully characterise this internal pore structure, SEM image processing proves insufficient, and XRμT was used. Two foaming processes that generate two distinct porous microstructures were studied. The scans being of lower resolution, direct cell identification is impossible, therefore an alternative statistical method was investigated. A new method based on 3D autocorrelation and the rose diagram was developed in order to measure characteristic lengths and anisotropy in the materials.

Results for the characteristic lengths are in good agreement with a visual inspection of the SEM scans, even for objects very small compared to the pixel size (2-3 pixels). Furthermore the rose diagram can provide a measure of the correlation variation in all direction, effectively measuring the degree of anisotropy in the structure. These very encouraging results are nuanced by the fact that a significant anisotropy is seen in both materials, even though the PMMA sample is supposed completely isotropic. This does not imply that the method produced erroneous results, but rather that it is sensitive to geometric distortions from the tomographic process. From the rose diagram we can only conclude to some form of anisotropy in the microstructure, but cannot link this directly to an elongation factor, nor deconvolute the influence of tomographic artefacts.

In order to better interpret the results of such a method, current work focuses on optimising the scanning parameters to obtain higher resolution tomograms and the development of a cell segmentation and separation algorithm. Figure 11 shows a recent reconstruction at 1.12 μm/pixel of the PMMA sample and initial cell separations carried out. Computing cell sizes and shape factors on these results can confirm measurements using the rose diagram.

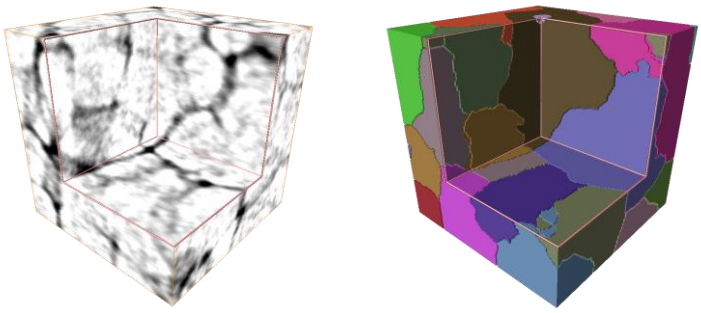

Figure 11. View of a 150µm subvolume of the PMMA sample at higher resolution (left) and preliminary results of a cell decomposition algorithm.

REFERENCES

BARUCHEL, J., BUFFIÈRE, J.-Y., MAIRE, E., MERLE, P., and PEIX, G., (2000), X-Ray Tomography in Material Science, Hermes Sciences Publications.

BLACHER, S., MAQUET, V., LÉONARD, A., CHAPELLE, G., CRINE, M., JÉRÔME, R., PIRARD, J.-P., (2002), Texture characterisation of ultramacroporous materials using non-destructive methods, Studies in Surface Science and Catalysis, 144, pp. 331-338.

BLACHER, S., CALBERG C., KERCKHOFS G., LÉONARD, A., WEVERS, M., JÉRÔME, R., PIRARD, J.-P., (2006), The porous structure of biodegradable scaffolds obtained with supercritical CO2 as foaming agent,
Studies in Surface Science and Catalysis, 160, pp. 681-688.

FELDKAMP, L. A., DAVIS, L. C. and KRESS, J.W., (1984), Practical conebeam algorithm, J. Opt. Soc. Am. A, 1, pp. 612–619.

HO-CHUL, L., JIN-YOUNG, K., CHANG-HO, N., KI YONG, S., and SUNG-HEON, C., (2006), Selective metal pattern formation and its EMI shielding efficiency. *Applied Surface Science*, 252, 8, pp.2665-2672.

KETCHAM, R.A. and RYAN, T.M., (2004), Quantification and visualization of anisotropy in trabecular bone. *Journal of Microscopy*, 213, 2, pp.158-171.

LÉONARD, A., CALBERG, C., KERCKHOFS, G., WEVERS, M., JÉRÔME, R., PIRARD, J.-P., GERMAIN, A., BLACHER, S. (2008), Characterization of the porous structure of biodegradable scaffolds obtained with supercritical CO_2 as foaming agent, *Journal of Porous Materials*, 15, pp. 397-403.

MAQUET, V., BLACHER, S., PIRARD, R., PIRARD, J.-P., VYAKARNAM, M. N., and JÉRÔMME, R., (2003). Preparation of macroporous biodegradable poly(l-lactide-co-ϵ-caprolactone) foams and characterization by mercury intrusion porosimetry, image analysis, and impedance spectroscopy. *J. Biomed. Mater. Res.*, 66A, 2, pp.199-213.

MOLENBERG, I., HUYNEN, I., BAUDOUIN, A.-C., BAILLY, C., THOMASSIN, J.-M. AND DETREMBLEUR, C., (2010), Foamed Nanocomposites for EMI Shielding Applications, In: M. MUKHERJEE, *Advanced Microwave and Millimeter Wave Technologies: Semiconductor Devices Circuits and Systems*, InTech, pp. 453-470.

WEHRLI, F., VASILIC, B., SAHA P., AND WALD, M., (2006), Performance comparison of the spatial autocorrelation function and the mean intercept-length in the determination of trabecular bone anisotropy in the in vivo environment, *Proceedings of the 14th Annual Meeting of ISMRM.*